Dynamic Simulation of Off-Grid Energy Island with Wind-PV-Storage Hydrogen Production

Li Zuo[1] Yuanhui Dong[1] Shubin Zhang[1] Yuxin Li[1] Haiming Zhang[1] Ji Ding[1] Qi Liu[1] Fanli Zhou[1] Liping Chen[2]

[1]Suzhou Tongyuan Software & Control Technology Co., Ltd, China, {zuoli, dongyuanhui, zhangsb, liyuxin, zhanghm, dingj, liuq, zhoufl}@tongyuan.cc
[2]Huazhong University of Science and Technology, Wuhan, China, chenlp@hust.edu.cn

Abstract

This study proposes a novel discrete-solving algorithm implemented on the MWORKS.Sysplorer platform for power electronics simulation, addressing dynamic stability challenges in multi-energy integrated systems with high renewable energy penetration. For an offshore energy island, detailed component models including direct-drive wind turbines, photovoltaics, battery energy storage, and alkaline electrolyzers are developed and integrated into a standalone DC system. The energy storage system controls bus voltage to enable constant-power operation of electrolyzers. The implemented discrete algorithm provides critical multi-timescale simulation capabilities, advancing the planning and construction of offshore energy island projects.

Keywords: modelica, discrete algorithm, offshore energy island, integrated energy systems, electrolyzer

1 Introduction

The global energy structure has been undergoing rapid decarbonization and sustainable transformation recently. As an emerging paradigm for large-scale renewable energy integration, offshore energy islands have garnered significant attention due to their ability to synergistically couple diverse energy forms, including offshore wind, solar photovoltaics (PV), energy storage, and hydrogen production (wind-solar-storage-hydrogen) into a unified system. Offshore wind power demonstrates superior energy generation efficiency and economic viability compared to its onshore counterparts (Bilgili, Yasar, and Simsek 2011), attributed to its higher wind energy density and more stable operating conditions. Unlike conventional offshore wind platforms, offshore energy islands not only improve renewable energy utilization and reduce long-distance transmission losses but also enable dynamic multi-energy coordination through integrated "electricity-hydrogen" solutions, thus delivering stable and clean energy supplies to coastal and island regions (Igbinenikaro, Adekoya, and Etukudoh 2024).

However, the high proportion of renewable energy sources poses significant challenges to the transient stability and operational security of energy island systems. Under islanded or weak grid conditions, power electronic converter-dominated energy conversion substantially reduce system equivalent inertia, leading to frequent fluctuations in voltage and power, diminished stability margins, and potential risks of equipment overload or operational failure—critical threats to system reliability. (Kundur 2007)(Salmador Gonzalez 2016). To mitigate the stochastic fluctuations of renewable generation, water electrolysis for hydrogen production has emerged as a key flexibility resource for offshore energy islands, using its high energy density and large-scale regulation capacity. By converting surplus wind/PV power into storable hydrogen, this technology enables rapid energy release during peak demand or power deficits, providing essential power buffering and dynamic support to enhance system stability (Arsad et al. 2022)(Xing et al. 2018)(Sterner 2009).

Current research predominantly focuses on optimizing integrated energy dispatch strategies to address renewable intermittency, particularly through adaptive operational mode adjustments for hydrogen production systems. Coordinated multi-electrolyzer switching strategies (Fang and Liang 2019) have been proposed to balance fluctuating wind/PV power. Subsequent studies have refined these approaches to minimize electrolyzer cycling, such as rotational coordination (Xiaojun, Congying, and Hong 2021), duty-cycling optimization (Shen et al. 2018), and start-stop frequency reduction (Tiejiang et al. 2022). Nevertheless, these dispatch-oriented optimizations often overlook critical equipment operational characteristics, limiting their applicability to real-world implementations. Consequently, high-fidelity modeling and simulation of actual energy island components are imperative to bridge this gap between theoretical strategies and engineering practices.

Modelica exhibits unique advantages in multi-physics unified modeling, facilitating detailed equipment-level simulations. Previous studies (Webster and Bode 2019) have developed proton exchange membrane (PEM) electrolyzer models using Modelica, achieving close alignment with experimental results. To further investigate electrochemical dynamics, dedicated libraries like the Electrochemical Reactors Library (Pyschik et al. 2025) have been established. However, existing research pre-

dominantly focuses on standalone electrolyzer modeling, lacking co-simulation frameworks integrating renewable generation sources. Moreover, when interfacing electrolyzers with power grids, most Modelica-based tools face inherent limitations in handling complex dynamic processes. First, in nanosecond-to-microsecond timescale simulations, frequent power electronic switching induces high-frequency dynamics that may trigger numerical oscillations and poor real-time performance. Second, the absence of specialized high-frequency model libraries for power electronic systems within the Modelica ecosystem necessitates manual development of fundamental components, increasing modeling complexity and compromising simulation efficiency.

This study leverages the MWORKS. Sysplorer platform—a Modelica-based system modeling and simulation tool developed by Suzhou Tongyuan Soft Control Technology Co., Ltd.—to construct a high-fidelity offshore energy island model. The platform's advanced electromagnetic transient solver and domain-specific libraries enable precise modeling of key components, including wind turbines, PV arrays, lithium-ion battery storage, and alkaline electrolyzers. The proposed system supports multi-timescale simulations of power system dynamics, providing robust technical validation for parameter optimization and control strategy development in offshore energy island projects.

2 Model Components

2.1 Direct-Drive Wind Turbine

As shown in Figure 1, the topology of a conventional direct-drive wind turbine system typically consists of three key components: wind turbine blades, a permanent magnet synchronous generator (PMSG), and a power converter along with its controller.

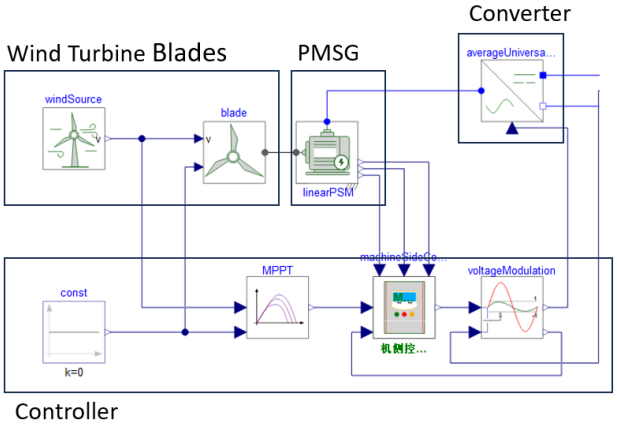

Figure 1. Topology of a conventional direct-drive wind turbine system

Based on aerodynamic theory, the mechanical power output of the wind turbine P_m can be calculated as:

$$P_m = \frac{1}{2} C_p(\lambda, \beta) \rho \pi R^2 v^3 \tag{1}$$

where, C_p is power coefficient, representing wind energy conversion efficiency; λ is the tip-speed ratio; β is blade pitch angle; ρ is the air density; R is rotor radius; v is the wind speed.

The power coefficient C_p, a critical parameter characterizing turbine efficiency, is expressed as a function of β and λ:

$$C_p = c_1 \left(\frac{c_2}{\lambda_i} - c_3 \beta - c_4 \beta^{c_5} - c_6 \right) e^{-\frac{c_7}{\lambda_i}} \tag{2}$$

$$\frac{1}{\lambda_i} = \frac{1}{\lambda + c_8 \beta} - \frac{c_9}{\beta^3 + 1} \tag{3}$$

where $c_1 - c_9$ are curve-fitting parameters that vary slightly across different turbine designs.

The drive train is modeled using a single-mass formulation:

$$H \frac{\mathrm{d}\omega_r}{\mathrm{d}t} = T_m - T_e \tag{4}$$

where, H is the total rotational inertia of the direct-drive system; T_m is the mechanical torque; T_e is the electromagnetic torque.

In the synchronous rotating dq-reference frame, the voltage equations are:

$$\begin{cases} L_s \dfrac{\mathrm{d}i_d}{\mathrm{d}t} = u_d - R_s i_d + \omega_s L_s i_q \\ L_s \dfrac{\mathrm{d}i_q}{\mathrm{d}t} = u_q - R_s i_q - \omega_s L_s i_d + \omega_s \psi_f \end{cases} \tag{5}$$

where, L_s is the stator inductance; R_s is the stator resistance; u_d, u_q are d- and q-axis stator voltages; i_d, i_q are d- and q-axis stator currents; ψ_f is the permanent magnet flux linkage; ω_s is the synchronous rotational speed.

The electromagnetic torque T_e is governed by:

$$T_e = \frac{3}{2} n_p \left[\psi_f i_q + (L_d - L_q) i_d i_q \right] \tag{6}$$

where n_p is the Number of pole pairs.

The operating range of a wind turbine generator can generally be divided into four regions: Pre-cut-in standby phase, maximum power point tracking (MPPT) phase, constant speed transition phase, and rated power regulation phase. In the maximum power point tracking phase, the rotational speed of the wind turbine is less than the maximum allowable speed. An optimal torque control mechanism, known as the Maximum Power Point Tracking (MPPT) system, is implemented to ensure that the wind turbine operates at the maximum wind energy utilization coefficient.

DOI
10.3384/ecp218909

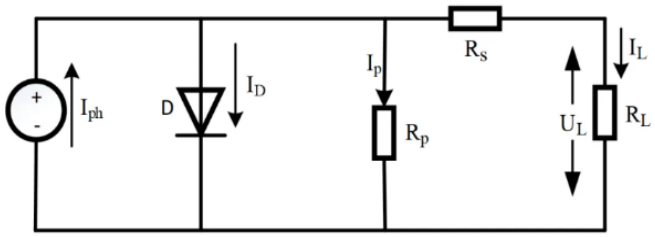

Figure 2. Photovoltaic equivalent circuit schematic

2.2 Photovoltaic

Photovoltaic power can be equated to a photovoltaic current source, a parallel diode, a series resistor R_s, and a parallel resistor R_p, as shown in Figure 2.

The output current I and photogenerated current I_{ph} relationships in photovoltaic systems are given by:

$$I = I_{ph} - I_s\left(e^{\frac{(V+IR_s)}{NV_t}} - 1\right) - \frac{V+IR_s}{R_p} \tag{7}$$

$$I_{ph} = I_{ph0}\frac{I_r}{I_{r0}} \tag{8}$$

where, I_r is the photogenerated current under actual irradiation; I_{ph0} is the reference photogenerated current at standard test conditions; I_s is the diode reverse saturation current; N is the diode ideality factor; V is the output voltage.

In practical PV systems, photovoltaic arrays are constructed through series-parallel configurations of multiple PV modules to meet diverse load power requirements. The system employs a Perturbation and Observation method (P&O) MPPT control strategy (Figure 3). The P&O method periodically perturbs the operating voltage slightly, then compares power before and after perturbation: continuing the direction if power increases, reversing it if power decreases. This iteration adapts to irradiance and temperature changes that shift the maximum power point, enabling stable tracking through the "perturb-and-observe" cycle. It keeps PV modules operating optimally, maintaining maximum power extraction and enhancing system efficiency under fluctuating conditions.

2.3 Energy Storage Battery

The equivalent circuit of the storage battery consists of a signal voltage source, a parallel self-discharge resistor R_{SD}, a charging dynamic model, and a series resistor R_0. The model's base voltage-charge state equation is described by the following equation:

$$V = V_0\left(\frac{SOC}{1-\beta(1-SOC)}\right) \tag{9}$$

where SOC is the ratio of the current charge to the rated capacity; V_0 is the voltage of a fully charged battery with no load; β is a constant that ensures the voltage equals V_1 when the charge is Ah_1. V_1 and Ah_1 can be given

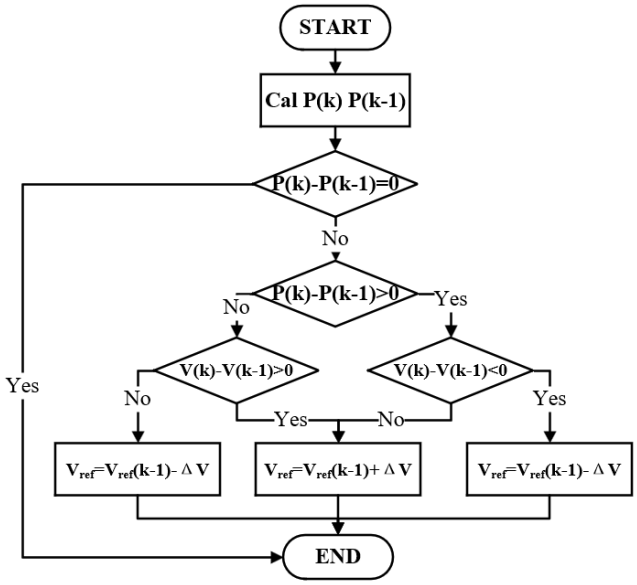

Figure 3. Perturbation and Observation method

through parameter setting, Ah_1 is the charging capacity/charge quantity corresponding to the voltage V_1 under no load, and V_1 is less than the rated voltage.

In energy storage control, the energy storage battery adopts voltage and current dual-loop control, and switches the charging and discharging states of the energy storage battery by outputting control signals. The voltage loop serves as the outer loop, taking the system's DC bus voltage as the control target. It compares the actual voltage with a preset reference voltage, and after processing the deviation through a PI regulator, outputs a current reference value. The current loop functions as the inner loop, which takes the current reference value output by the voltage loop as its target and eliminates the deviation between the actual current and the reference current via PI regulation, thereby generating precise control signals to regulate the charging and discharging processes.

2.4 Alkaline Electrolyzer

During electrolysis, DC power is applied across two electrodes in the electrolyte:

- Anode (Oxidation):

$$4OH^- \rightarrow O_2\uparrow + 2H_2O + 4e^-$$

- Cathode (Reduction):

$$2H_2O + 2e^- \rightarrow H_2\uparrow + 2OH^-$$

The rate of an electrolytic cell reaction is closely related to the current in the cell. According to Faraday's law (Ulleberg 2003), the rate of production of oxygen and hydrogen is directly proportional to the current I passing

through the electrolyzer, according to the following equation:

$$\begin{cases} \dot{N}_{\mathrm{O_2}} = \dfrac{I}{4F} & \text{(Oxygen production rate)} \\ \dot{N}_{\mathrm{H_2}} = \dfrac{I}{2F} & \text{(Hydrogen production rate)} \end{cases} \tag{10}$$

where, $\dot{N}_{\mathrm{O_2}}$ is the molar production rate of oxygen; $\dot{N}_{\mathrm{H_2}}$ is the molar production rate of hydrogen; I is the applied current; F is Faraday's constant (96,485 C/mol).

During the electrolysis of water, the anode and cathode follow the principle of mass conservation, respectively, which is used to describe the dynamic equilibrium between reactants and products:

$$\frac{dN_{H_2O}}{dt} = N_{H_2O}^{in} - N_{H_2O}^{out} + N_{H_2O}^{gn} \tag{11}$$

$$\frac{dN_{O_2}}{dt} = N_{O_2}^{in} - N_{O_2}^{out} + N_{O_2}^{gn} \tag{12}$$

$$\frac{dN_{H_2}}{dt} = N_{H_2}^{in} - N_{H_2}^{out} + N_{H_2}^{gn} \tag{13}$$

where, superscript *in* represents the inflow of substances; superscript *out* represents the outflow of substances; superscript *gn* represents the net generation of substances due to electrochemical reactions (a negative value indicates consumption in the reaction); suffix H_2O, O_2, H_2, respectively, represent water, oxygen, and hydrogen.

The total cell voltage consists of three components:

$$V_{\mathrm{cell}} = V_{\mathrm{rev}} + V_{\mathrm{act}} + V_{\mathrm{ohm}} \tag{14}$$

where, V_{rev} is the reversible voltage (thermodynamic equilibrium); V_{act} is the activation overpotential; V_{ohm}: Ohmic overpotential.

The reversible voltage is determined by thermodynamic equilibrium and is calculated by the Nernst equation (Bard, Faulkner, and White 2022), where the standard reversible voltage is empirically correlated (Roy, Watson, and Infield 2006), reflecting the theoretical minimum decomposition voltage:

$$V_{\mathrm{rev}} = V^0 + \frac{RT}{2F} \ln\left(\frac{p_{\mathrm{H_2}}^{1/2} p_{\mathrm{O_2}}^{1/4}}{a_{\mathrm{H_2O}}}\right) \tag{15}$$

where, V_{rev} is the reversible voltage, affected by temperature; $p_{\mathrm{H_2}}$ and $p_{\mathrm{O_2}}$ are the partial pressures of hydrogen and oxygen, respectively; $a_{\mathrm{H_2O}}$ is the activity of water.

The standard reversible voltage V_{rev}^0 is temperature-dependent:

$$\begin{aligned} V_{\mathrm{rev}}^0 = {} & 1.5148 - 1.5421 \times 10^{-3} T \\ & + 9.23 \times 10^{-5} T \ln T + 9.84 \times 10^{-8} T^2 \end{aligned} \tag{16}$$

The activation overpotential V_{act}, which overcomes the activation energy barrier for the electrochemical reaction at the electrode surface, is caused by electrochemical kinetics and is described by the Butler-Volmer equation (Falcão and Pinto 2020). Typically, the overpotential at the anode is higher than at the cathode:

$$V_{\mathrm{act}} = \frac{RT}{\alpha F} \ln\left(\frac{i}{i_0(1-\Theta)}\right) \tag{17}$$

where, i_0 is the exchange current density; i is the current density; Θ is the electrode surface gas coverage; α is the charge transfer coefficient.

The ohmic overpotential V_{ohm} arises from the internal resistance of the electrolyzer and follows Ohm's law:

$$V_{\mathrm{ohm}} = I \cdot R_{\mathrm{cell}} \tag{18}$$

where R_{cell} is the total resistance of the electrolyzer, including the electrolyte, electrodes, separator, and connecting components.

3 Modelica-Based Power Electronics Simulation

With the widespread integration of high-frequency switching power semiconductor devices in emerging power systems, the system exhibits multi-timescale dynamic behaviors, spanning from nanoseconds (switching transients) to seconds (system-level energy flow and control responses). Traditional Modelica-based power system modeling(Chieh, Panciatici, and Picard 2011) and simulation frameworks are increasingly challenged by the dual bottlenecks of modeling fidelity and computational efficiency(Masoom et al. 2021).

At the modeling level, idealized switch models fail to capture the nonlinear dynamic characteristics of switching transients, as they neglect critical device-level physical phenomena, such as junction capacitance, charge storage, and parasitic inductance. In contrast, physics-based detailed models (e.g., incorporating charge dynamics, temperature dependence, and parasitic networks) offer higher accuracy but are computationally prohibitive for large-scale system simulations.

At the simulation level, conventional variable-step integration algorithms rely on local error estimates to adjust step sizes. However, their gradual step-size reduction mechanisms struggle to effectively resolve both the abrupt transitions at switching events and the slow-varying dynamics of energy storage and thermal inertia components. Moreover, the presence of inherent parasitic parameters—such as stray inductances, device capacitances, and snubber networks—introduces significant numerical stiffness. This stiffness, characteristic of power electronic systems, exacerbates numerical oscillations, increases solver iteration counts, and severely impacts overall simulation speed and stability (Sterner 2009)(Li et al. 2017).

To address these challenges, Suzhou Tongyuan has focused on advancing solution algorithms for power electronic systems, leveraging fixed-step implicit methods as a

DOI 10.3384/ecp218909

foundation. Building on fixed-step implicit Euler and implicit trapezoidal algorithms, discrete forms of these methods have been developed to enhance simulation efficiency and resolve issues specific to discrete simulation, as illustrated in Figure 4.

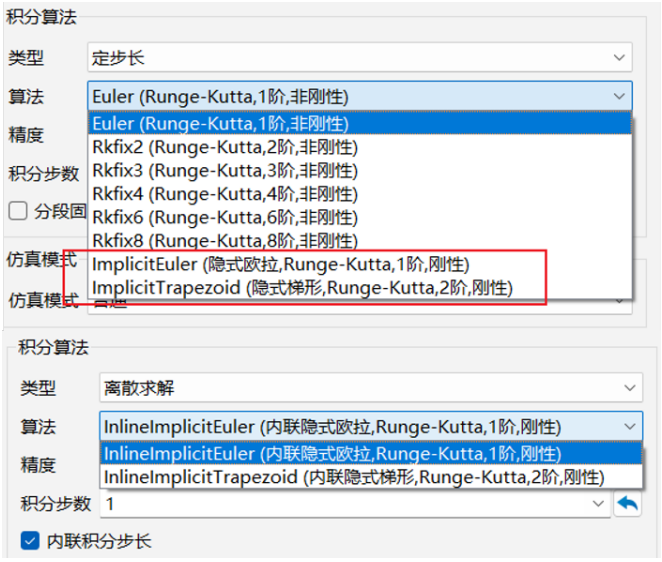

Figure 4. continuous and discrete solving algorithms

Specifically, the implicit Euler method and implicit trapezoidal rule, as core fixed-step implicit algorithms, possess unique properties that underpin their application in power electronic simulations:

The implicit Euler method is based on backward difference approximation, deriving the next-time-step state from the current-time-step state through the formula:

$$\frac{x_{k+1}-x_k}{h} = f(t_{k+1}, x_{k+1}) \tag{19}$$

It features first-order accuracy with strong numerical damping, which can effectively suppress high-frequency oscillations—an advantage when dealing with stiff systems induced by parasitic parameters. While its computational load is relatively low, its accuracy is limited.

The implicit trapezoidal rule combines derivative information from both the current and next time steps, employing trapezoidal integration approximation described by:

$$x_{k+1} = x_k + \frac{h}{2}\left[f(t_k, x_k) + f(t_{k+1}, x_{k+1})\right] \tag{20}$$

It offers second-order accuracy with weak numerical damping, enabling more accurate preservation of the system's inherent dynamic characteristics (e.g., transient oscillations in energy storage components). Though it provides higher accuracy, its computational load per iteration is slightly greater.

Sysplorer constructs a general mathematical model for power electronic system simulation based on the branching method and branching constitutive equations, supporting both continuous and discrete fixed-step algorithms. For discrete fixed-step schemes, the following key design strategies address numerical challenges:

1. Leveraging Piecewise Linear Time-Invariance
   During switching transients, the segmented analytical linearization technique decomposes the nonlinear switching process into multiple linear intervals. Within each interval, system dynamics are described by a linear state equation:

$$\dot{X} = A(t)X + B(t)U \tag{21}$$

   For such linear systems, the implicit Euler method is employed for discretization. Using the backward difference approximation for the time derivative, the discrete update rule is derived as:

$$\frac{X_{k+1}-X_k}{\Delta t} = A_{k+1}X_{k+1} + B_{k+1}U_{k+1} \tag{22}$$

   The core methodology for model discretization incorporates proprietary techniques protected by intellectual property rights and thus will not be elaborated in detail.

   Rearranging terms to solve for X_{k+1}, we obtain:

$$X_{k+1} = (I - \Delta t \cdot A_{k+1})^{-1} \cdot (X_k + \Delta t \cdot B_{k+1}U_{k+1}) \tag{23}$$

   Here, I denotes the identity matrix. This approach transforms state updates into a matrix inversion operation, exploiting the linear structure of the model to avoid nonlinear iterations. When solving the original model directly using the implicit Euler method or other implicit numerical integration algorithms, implicit methods require solving a nonlinear system of equations (the size of which is determined by the number of state variables). Efficiency issues may arise when the scale of this nonlinear system becomes excessively large. In contrast, this discretization method can leverage the inherent linear relationships of the model to further reduce the system equations, thereby improving simulation efficiency. For power electronic systems with inherent numerical stiffness (e.g., induced by parasitic capacitances or inductances), this strategy effectively mitigates numerical oscillations and convergence issues, enhancing the efficiency of fixed-step simulations.

2. **Accurate Switching Event Positioning**
   The discrete algorithms support precise detection of switching events (e.g., device turn-on/turn-off timing). By synchronizing state updates with event triggers, the simulation accuracy of fixed-step algorithms is further improved.

In Figure 5, the average model is based on the state averaging method to establish continuous time-domain

equations, and focuses on the low-frequency dynamic characteristics of the converter by filtering out the switching frequency ripples, which significantly reduces the order of the model to meet the demand for real-time simulation. For the high-frequency characterization of nanosecond switching transients, the detailed switching transient model adopts the segmented analytical linearization technique, which decomposes the switching process into multiple linearization intervals, and accurately characterizes the nonlinear behaviour of the device during the on/off process through the dynamic switching between analytical solving and event triggering. The three types of models are decoupled by time scale and interface variables to form a multi-level simulation framework from microsecond transient to second system response. Switching models are suitable for short-term high-precision analysis, while the averaging model is suitable for long-term or multi-component system simulations (Reindl et al. 2023).

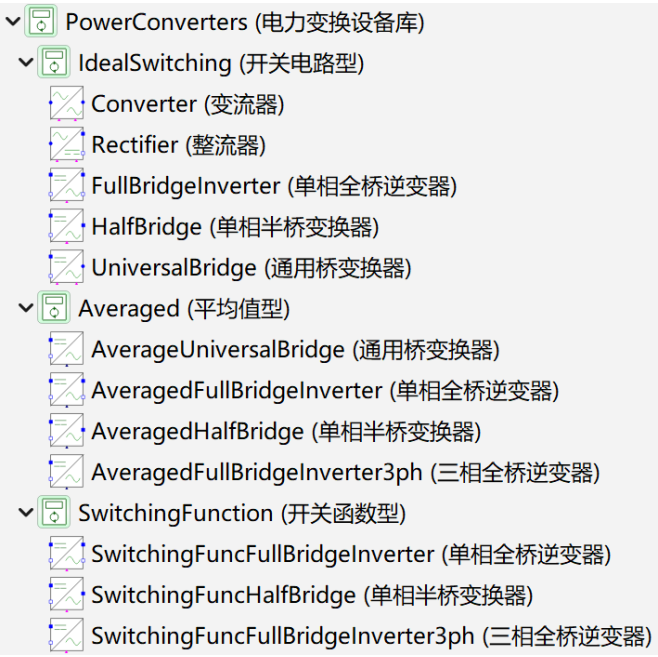

Figure 5. Power Electronic Converter Model

Based on the MWORKS.Sysplorer electromagnetic transient solving algorithm, the DC grid-connected model of the PV system in Figure 6 is calculated, and the simulation time is set to 0.5 s, the step size of the detailed switching model is 1×10^{-5} seconds, and the step size of the average value model is 5×10^{-5} seconds. The simulation results are consistent in terms of key performance variables, and a comparison of simulation times is presented in Table 1. The discrete algorithm incurs longer simulation time than the continuous counterpart. This stems from the model's frequent nonlinear switching events: although segmented linearization decomposes switching transients into linear intervals, repeated matrix inversions across these intervals accumulate computational overhead.

Considering the application scenario of off-grid energy islands, which integrate multiple distributed energy

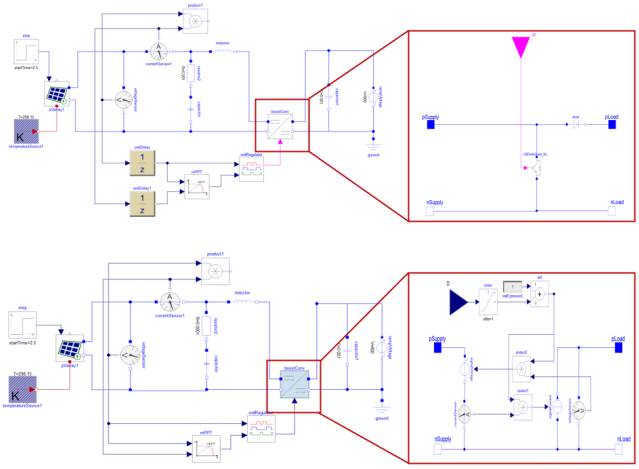

Figure 6. Test PV system for algorithm validation

sources, energy storage systems, and diverse loads with strong system coupling, long-term simulation is often required to analyze energy scheduling strategies, operational stability, and dynamic responses under fluctuating renewable energy inputs. In addition, considering issues such as system coupling and simulation rate, the average value model can meet the requirements of simulation accuracy. Therefore, the converter models in this paper all adopt the average value model.

4 System Modeling and Simulation

4.1 System Configuration

This chapter models an islanded DC microgrid integrating a photovoltaic (PV) system, wind power generation, electrochemical energy storage and an alkaline electrolyzer for hydrogen production. The system employs maximum power point tracking (MPPT) control to maximize renewable energy harvesting from PV and wind power, while a dual-loop adaptive control is implemented in the energy storage system to keep the DC bus voltage stable and smoothen the hydrogen production process. The alkaline electrolyzer is operated under constant power control to ensure optimal hydrogen production efficiency.

Figure 7 illustrates the operating flow of this renewable energy-hydrogen hybrid system. When the renewable energy generation exceeds the power demand of the electrolyzer, the excess energy is absorbed by the energy storage device. Conversely, when the load demand exceeds the renewable energy generation, the energy storage device discharges to compensate for the power deficit, thus maintaining the system in dynamic balance.

Component-level modeling takes a systematic approach: after initial independent validation of the wind, photovoltaic, and hydrogen generation subsystems, a full system simulation is performed with or without integrated energy storage. All simulations were performed using the discrete InlineImplicitEuler algorithm with a fixed time step of 5×10^{-5} seconds.

DOI
10.3384/ecp218909

Table 1. Comparison of Simulation Time for Different Converter Types and Algorithms

Converter Type	Simulation Time	
	Continuous Algorithm	Discrete Algorithm
Detailed Switching (step size: 1×10^{-5})	0.477	3.223
Average Model (step size: 5×10^{-5})	0.058	0.362

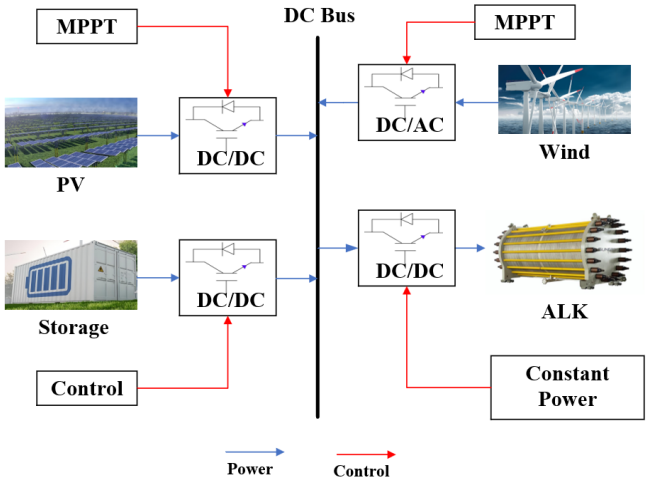

Figure 7. Schematic diagram of the structure of a Wind-PV-Storage Integrated Hydrogen Production system

4.2 Subsystem Validation

4.2.1 Wind Power System

According to Equation 1 – Equation 6 and the control method to establish the wind electronic system, as shown in Figure 8, the wind electronic system consists of wind speed model, blades, permanent magnet synchronous generator, averaged universal bridge converter, MPPT controller, voltage modulation model, machine-side controller and so on, and the main parameters of the wind power system are shown in Table 2.

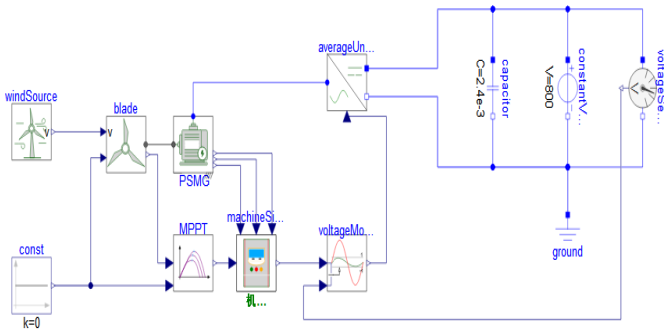

Figure 8. Model diagram of wind electronic system

The system employs a combined wind speed simulation to model the variation of wind speed over time. The wind speed starts from an initial value of 3 m/s and gradually increases to 9 m/s, taking into account both gradual wind changes and random wind fluctuations. The simulation duration is set to 500 seconds.

Table 2. Wind Turbine Parameters

Parameter	Value/Unit
Rated Power P	2 MW
Rated Speed ω	1.93 rad/s
Blade Radius R	40 m
Blade Pitch Angle β	0 °
Air Density ρ	1.293 kg/m^3
Wind Energy Calculation Coefficients	0.70, 150, 0.58, 0.002, 2.12, 13, -18, -0.02, 0.003

The results of the blade wind energy and mechanical power calculations are shown in Figure 9. It can be observed that the wind turbine operates in the constant speed region of the power tracking curve. The pitch angle β is maintained at 0 degrees, indicating normal turbine operation. However, the mechanical power has not reached the rated value, implying that a significant portion of the wind energy is not fully captured. The pitch angle remains unchanged, and the power output is primarily determined by the wind speed and the aerodynamic performance of the blades.

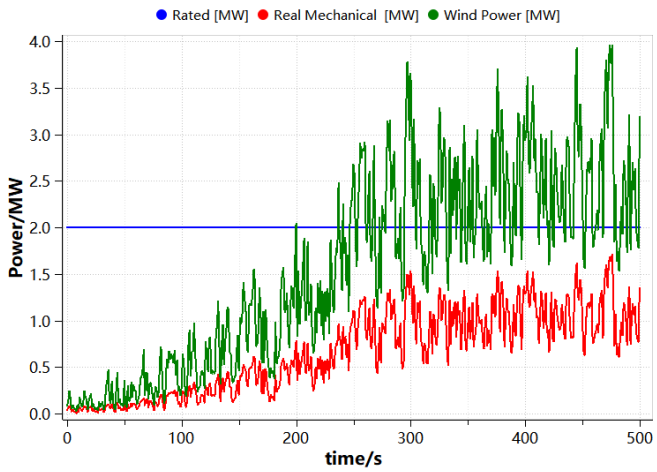

Figure 9. Wind and mechanical power curves

As shown in Figure 10, the tip-speed ratio and power coefficient curve indicate that the system has successfully

implemented Maximum Power Point Tracking (MPPT). The power coefficient has reached its maximum value, and the actual tip-speed ratio of the wind turbine closely approximates the optimal tip-speed ratio corresponding to the maximum power coefficient. The deviation of the tip-speed ratio from its optimal value is attributed to the fact that wind speed is not directly measured. Consequently, the reference signal for the controller (i.e., the rotational speed of the wind turbine) cannot directly respond to wind speed variations.

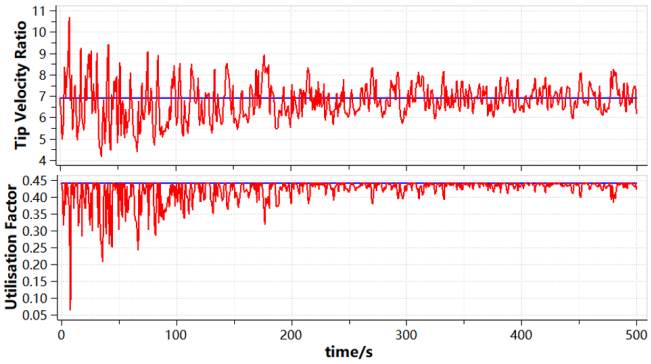

Figure 10. Leaf tip speed ratio curve and wind energy utilisation curve

4.2.2 Photovoltaic System

The photovoltaic (PV) system is established based on Equation 7−Equation 8 and the MPPT control method, as shown in Figure 11. The system comprises environmental models, PV panels, a Boost converter with an MPPT controller, etc. The Boost converter employs an average model and steps up the voltage based on the duty cycle signal output from the voltage regulator.

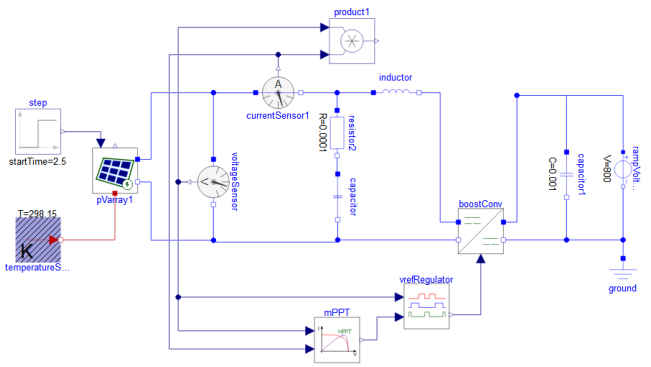

Figure 11. Photovoltaic power generation system

The solar irradiance is set to 1,000 W/m² and steps up to 1,200 W/m² at 2.5 s. The temperature is maintained at 25 °C. Each PV panel has a rated power of 213.15 W, with 10 panels connected in series and 47 panels connected in parallel. The main parameters of the single PV panel are listed in Table 3.

The photovoltaic (PV) MPPT control system can track environmental changes and adjust the output voltage of the PV array to maximize the output power.

Table 3. Single PV Panel Parameters

Parameter	Value/Unit
Maximum Power P_{max}	213.15 W
Number of Cells N_{cell}	60
Open-Circuit Voltage V_{oc_user}	36.3 V
Operating Voltage V_{mp_user}	29 V
Short-Circuit Current I_{sc_user}	7.84 A
Maximum Power Point Current I_{L_ref}	-0.36099 A
Voltage Temperature Coefficient β_{v_user}	0.102 V/K
Current Temperature Coefficient β_{i_user}	0.102 A/K
Series Resistance R_{s0}	0.39381 Ω
Shunt Resistance R_{sh0}	313.0553 Ω

As shown in Figure 12, the output power of the PV array varies with solar irradiance. The simulation results indicate that when the solar irradiance increases from 1,000 W/m² to 1,200 W/m², the output power of the PV panel, controlled by the MPPT controller, increases from 102,169 W to 121,362 W. This demonstrates that the MPPT controller effectively tracks environmental changes and stabilizes the output power at the maximum power point.

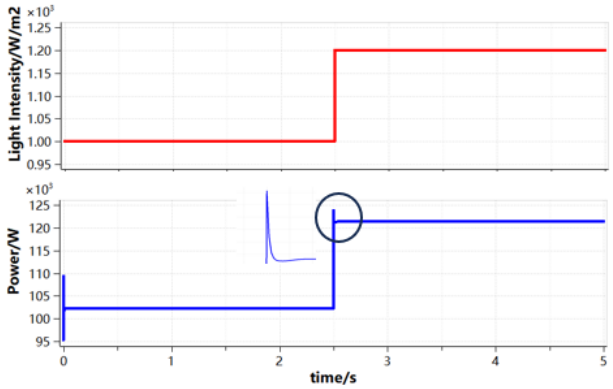

Figure 12. Variation curve of PV array output power with solar irradiance

4.3 Alkaline Electrolyzer

The alkaline electrolyzer model is established based on Equation 10−Equation 18. Considering the high reusability of the electrolyzer model, separate modeling is performed for the cathode, anode, Anolyte, Catholyte and separator within the alkaline electrolyzer. Based on the principles of alkaline electrolysis and considering current flow and material movement, the components are connected via electrolyzer ports and fluid interfaces.

The internal pressure of the electrolyzer is set to 1 bar, with the temperature maintained at 353 K, and temperature variations are considered negligible. A fixed voltage of 2 V is applied to a single electrolyzer cell for electrol-

ysis, with a current density of 1470 A/m^2. The potential differences between the components are listed in Table 4.

Table 4. Potential Differences Between Electrolyzer Components

Component	Potential Difference
Anode	0.57V
Anolyte	0.25V
Separator	0.02V
Catholyte	0.17V
Cathode	0.99V

The hydrogen and oxygen production rates of the alkaline electrolyzer are depicted in Figure 13. The production rates stabilize after 3 seconds. The balance time is influenced by the initial volume of the solution in the electrolyzer and the flow rate of the solution entering the electrolyzer. The hydrogen production rate per cell is 0.1678 Nm^3/h, while the oxygen production rate is 0.0838 Nm^3/h.

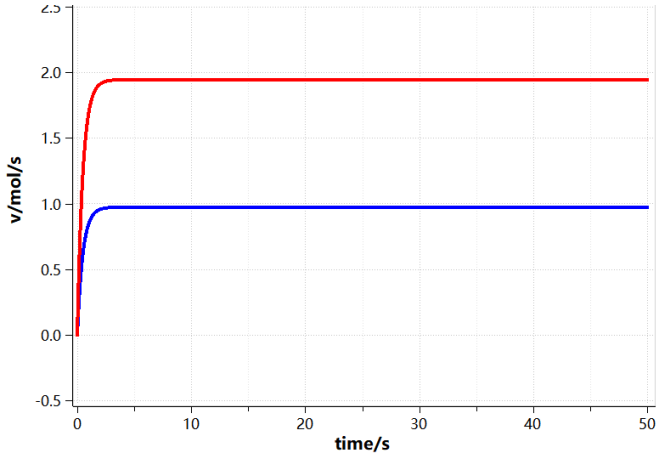

Figure 13. Hydrogen and oxygen production rates

4.4 Wind Power Storage Hybrid System Simulation

To validate the effectiveness of the hybrid wind–photovoltaic–storage hydrogen production system model and its control strategy for an offshore energy island scenario, and to analyze the impact of the wind and PV maximum power point tracking (MPPT) control strategy and the energy storage unit on system reliability and stability, simulations of the wind–PV hydrogen production system were conducted in two scenarios: with and without an energy storage unit.

4.5 Wind-Photovoltaic Hydrogen Production System Simulation

Based on the aforementioned wind power, photovoltaic, and alkaline electrolyzer models and their corresponding control strategies, a hybrid wind–PV hydrogen production system was established. The system comprises 100 series-connected alkaline electrolyzers, with a total rated power of 100 kW. The wind power and PV parameters were appropriately adjusted to match the rated power with the electrolyzer's hydrogen production load. Wind and PV power, as the source side, exhibit significant complementary characteristics in terms of temporal and spatial properties. Variations in wind speed and solar irradiance were simulated to verify the performance of the hybrid wind–PV power generation system under different operating conditions. The system configuration is illustrated in Figure 14.

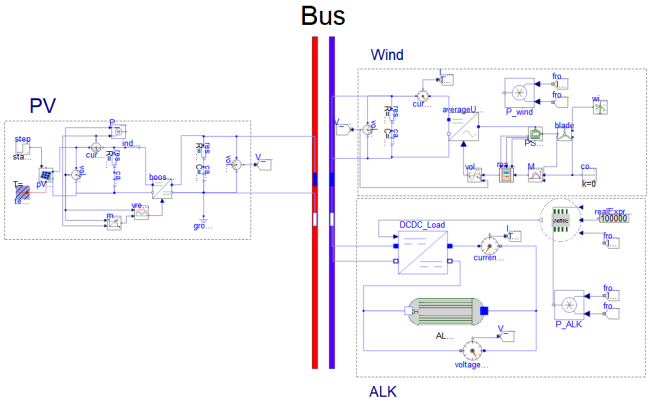

Figure 14. Hybrid Wind-PV Hydrogen Production System Topology

By adjusting the input of solar irradiance and wind speed, the initial solar irradiance was set to 800 W/m^2 and increased to 1000 W/m^2 at 100 s. The wind speed profile incorporated gusts, gradual changes, and random fluctuations.

As shown in Figure 15, the PV MPPT controller rapidly stabilizes the power output at the maximum power point. In the early simulation phase (first 100 s), the alkaline electrolyzers operates at low power due to insufficient wind–PV power generation. After the solar irradiance increase at 100 s, the electrolyzer's power gradually approaches 100 kW. However, as the wind power output further increases during the maximum power point tracking phase, the electrolyzer's power exceeds its rated capacity, posing potential safety concerns.

The fluctuations in wind and PV power generation significantly impact the safe operation of the alkaline electrolyzer. Due to the instability of wind and PV power, the input power to the electrolyzer may experience significant fluctuations, making it challenging to configure the electrolyzer capacity for specific scenarios.

4.6 Wind-PV-Storage Hydrogen Production System Simulation

To address the issues identified in the previous section, an energy storage system is coupled with the hybrid wind–wind-photovoltaic hydrogen production system. The energy storage system adaptively balances the power output

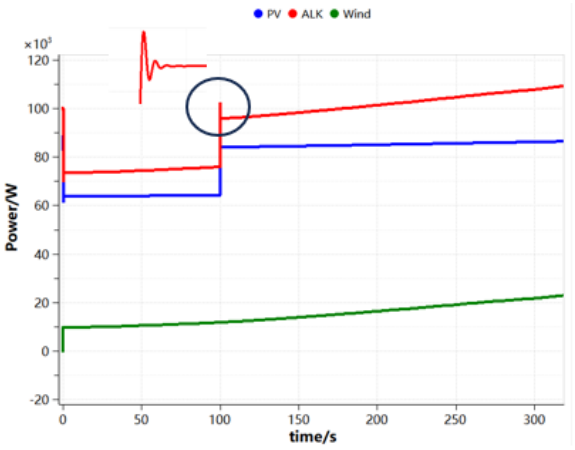

Figure 15. Wind-PV and Electrolyzer Power

from the wind and photovoltaic sources, suppressing fluctuations and stabilizing the DC bus voltage. This ensures that the electrolyzer operates stably at its rated power. The simulation model of the system is shown in Figure 16. The energy storage system is configured with a capacity of 38.4 kWh and an initial state of charge (SOC) of 0.5, and the simulation time is set to 1000 seconds.

The adaptive coordinated control of the energy storage system is based on the DC bus voltage as the power control signal, employing dual-loop voltage and current control. Photovoltaic and wind power, as renewable energy sources, have priority in power output. When the output power is higher or lower than the rated power of the alkaline electrolyzer load, the energy storage system achieves charging and discharging functions through an adaptive coordinated control method. This maintains the balance of the DC bus voltage and ensures the stable and safe operation of the electrolyzer.

In a 1000-second simulation period, the irradiance random perturbation condition was set (irradiance range: 500 - 2000 W/m², step interval: 100 seconds). Figure 17 shows that when an energy storage unit system adaptive coordinated control is activated to maintain the bus voltage at 800 V, small fluctuations in bus voltage occur with each irradiance fluctuation. The magnitude of these voltage fluctuations is related to the extent of irradiance changes. Despite these small fluctuations, the bus voltage remains relatively stable.

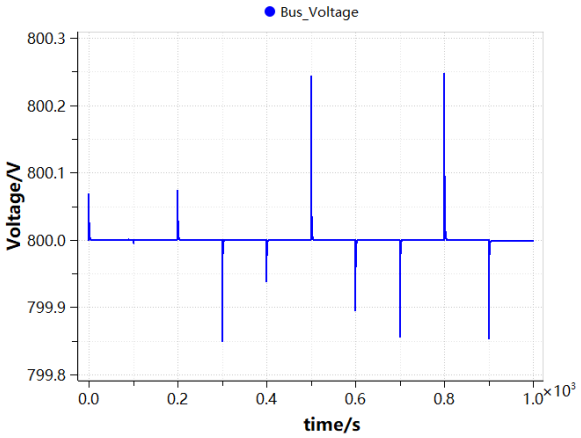

Figure 17. DC bus Voltage

The stable bus voltage enables the alkaline electrolyzer's constant-power controller to operate stably and continuously. The fluctuations in wind and solar power are both smoothed out by the energy storage system, as shown in Figure 18. Within the simulation period, the wind power output increases slowly but remains relatively low, so the system is mainly powered by solar energy. When the solar power output changes abruptly, the en-

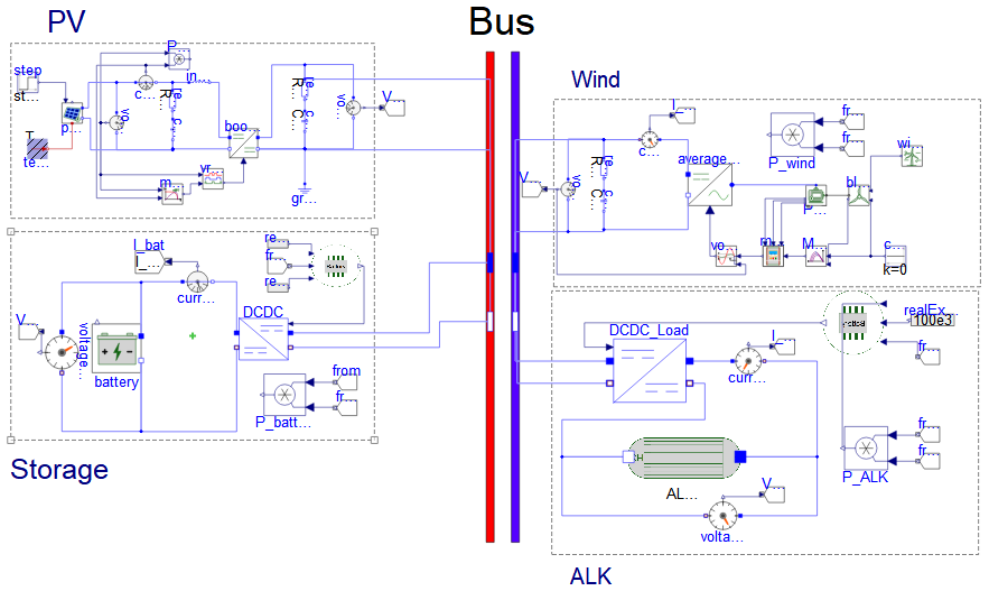

Figure 16. Hybrid Wind-PV-Storage Hydrogen Production System Topology

DOI
10.3384/ecp218909

ergy storage system responds by stabilizing it. The energy storage system's charge or discharge state is determined by the power difference between renewable outputs and the electrolyzer's 100 kW set power. The corresponding state-of-charge (SOC) variation is presented in Figure 19

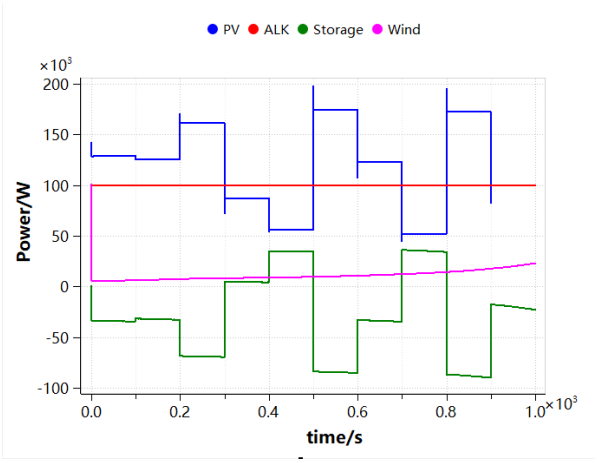

Figure 18. Wind-PV-Storage and Electrolyzer Power

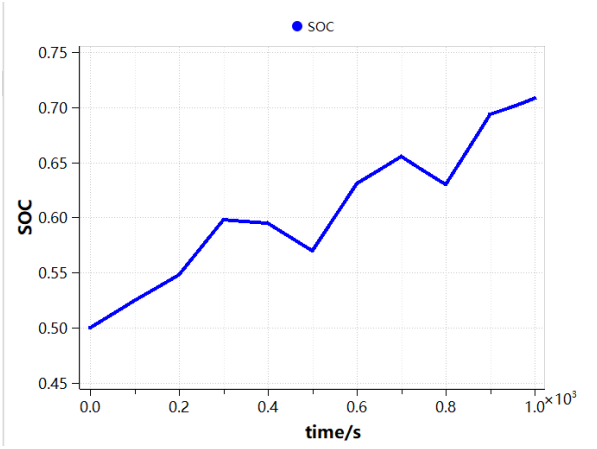

Figure 19. Energy storage SOC

The hydrogen and oxygen production rates of 100 series-connected alkaline electrolyzers with a rated power of 100 kW are shown in Figure 20. Under a current density of 1916 A/m^2 and a cell voltage of 2.087 V, the hydrogen and oxygen production rates are 20 Nm^3/h and 10 Nm^3/h, respectively.

5 Conclusions and Outlook

This paper investigates the dynamic characteristics and control strategies of an offshore energy island system in a hybrid wind–photovoltaic–energy storage hydrogen production scenario through detailed modeling and simulation based on Modelica. The key findings are summarized as follows:

Three modeling methods with different granularities are proposed for the multi-time-scale dynamic response problem of power electronic systems, and continuous and

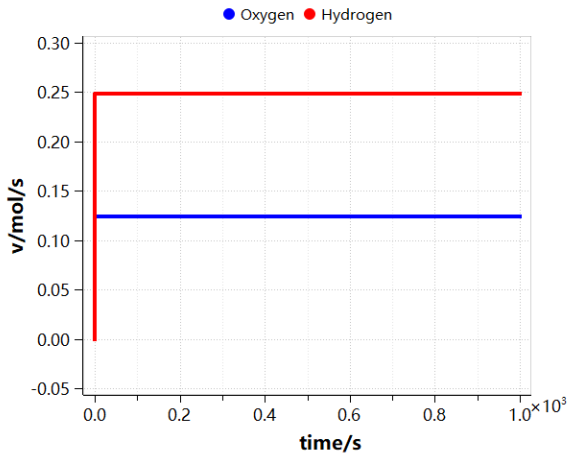

Figure 20. Hydrogen and oxygen production rates

discrete solution algorithms are developed. These approaches significantly enhance simulation efficiency and accuracy.

Subsystem verification shows that the wind power system achieves effective wind energy capture through maximum power point tracking (MPPT) control, and the photovoltaic system.

The energy storage system effectively mitigates the volatility of wind and photovoltaic power generation, maintains DC bus voltage stability, and ensures the safe operation of the electrolyzer.

The research results provide a high-precision simulation support for system parameter optimization and control strategy verification of offshore energy islands, offering significant reference value for practical project implementation. Future work could further explore the system's dynamic behavior across multiple time scales and complex electromagnetic transient processes to enhance the overall performance of offshore energy islands. Additionally, the proposed framework can be extended to include detailed models for hydrogen storage and ammonia/methanol production, bridging the gap between power systems and chemical processes.

References

Arsad, A Zaini et al. (2022). "Hydrogen energy storage integrated hybrid renewable energy systems: A review analysis for future research directions". In: *International Journal of Hydrogen Energy* 47.39, pp. 17285–17312.

Bard, Allen J, Larry R Faulkner, and Henry S White (2022). *Electrochemical methods: fundamentals and applications*. John Wiley & Sons.

Bilgili, Mehmet, Abdulkadir Yasar, and Erdogan Simsek (2011). "Offshore wind power development in Europe and its comparison with onshore counterpart". In: *Renewable and Sustainable Energy Reviews* 15.2, pp. 905–915. ISSN: 1364-0321. DOI: https://doi.org/10.1016/j.rser.2010.11.006. URL: https://www.sciencedirect.com/science/article/pii/S1364032110003758.

Chieh, Angela S., Patrick Panciatici, and Jérôme Picard (2011). "Power system modeling in Modelica for time-domain simulation". In: pp. 1–8. DOI: 10.1109/PTC.2011.6019400.

Falcão, DS and AMFR Pinto (2020). "A review on PEM electrolyzer modelling: Guidelines for beginners". In: *Journal of cleaner production* 261, p. 121184.

Fang, Ruiming and Yin Liang (2019). "Control strategy of electrolyzer in a wind-hydrogen system considering the constraints of switching times". In: *International journal of hydrogen energy* 44.46, pp. 25104–25111.

Igbinenikaro, Osayi Philip, Oladipo Olugbenga Adekoya, and Emmanuel Augustine Etukudoh (2024). "Conceptualizing sustainable offshore operations: Integration of renewable energy systems". In: *International Journal of Frontiers in Science and Technology Research* 6.02, pp. 031–043.

Kundur, Prabha (2007). "Power system stability". In: *Power system stability and control* 10.1, pp. 7–1.

Li, Boyang et al. (2017). "A novel simulation method for power electronics: Discrete state event driven method". In: *CES Transactions on Electrical Machines and Systems* 1.3, pp. 273–282.

Masoom, A. et al. (2021). "Modelica-based simulation of electromagnetic transients using Dynao: Current status and perspectives". In: *Electric Power Systems Research* 197, p. 107340. ISSN: 0378-7796. DOI: https://doi.org/10.1016/j.epsr.2021.107340. URL: https://www.sciencedirect.com/science/article/pii/S0378779621003217.

Pyschik, Jan F et al. (2025). "eCherry: A Modelica Library for Modular Dynamic Modelling of Electrochemical Reactors". In: *Electrochemical Science Advances*, e202400030.

Reindl, Andrea et al. (2023). "Switching and Averaging Models of a Bidirectional, Half-Bridge Based DC-DC converter with Load Distribution". In: pp. 683–692.

Roy, Amitava, Simon Watson, and David Infield (2006). "Comparison of electrical energy efficiency of atmospheric and high-pressure electrolysers". In: *International Journal of Hydrogen Energy* 31.14, pp. 1964–1979.

Salmador Gonzalez, Juan (2016). "Frequency support by variable speed wind turbines in the power system of Gran Canaria". In.

Shen, Xiaojun et al. (2018). "Experimental study on the external electrical thermal and dynamic power characteristics of alkaline water electrolyzer". In: *International journal of energy research* 42.10, pp. 3244–3257.

Sterner, Michael (2009). *Bioenergy and Renewable Power Methane in Integrated 100% Renewable Energy Systems. Limiting Global Warming by Transforming Energy Systems: Limiting Global Warming by Transforming Energy Systems*. Vol. 14. kassel university press GmbH.

Tiejiang, Yuan et al. (2022). "The day-ahead output plan of hydrogen production system considering the start-stop characteristics of electrolytic cell". In: *Electric power* 55.1, p. 101.

Ulleberg, Øystein (2003). "Modeling of advanced alkaline electrolyzers: a system simulation approach". In: *International Journal of Hydrogen Energy* 28.1, pp. 21–33. ISSN: 0360-3199. DOI: https://doi.org/10.1016/S0360-3199(02)00033-2. URL: https://www.sciencedirect.com/science/article/pii/S0360319902000332.

Webster, John and Carsten Bode (2019). "Implementation of a non-discretized multiphysics PEM electrolyzer model in modelica". In: *13th International Modelica Conference 2019*. Linköping University Electronic Press, pp. 833–840.

Xiaojun, Shen, Nie Congying, and Lü Hong (2021). "Coordination control strategy of wind power-hydrogen alkaline electrolyzer bank considering electrothermal characteristics". In: *Transactions of China Electrotechnical Society* 36.3, pp. 463–472.

Xing, Xuetao et al. (2018). "Modeling and operation of the power-to-gas system for renewables integration: a review". In: *CSEE Journal of Power and Energy Systems* 4.2, pp. 168–178.